Aspirating Cell into Orifice of Micropipette for Precise Cell Transportation Using Micropipette

Xiangfei Zhao, Mingzhu Sun, Qili Zhao, Yaowei Liu, Yidi Zhang, Bingxin Li, Xin Zhao

***Abstract*— Single-cell transportation is one of the most common cell operations. Transporting cells with micropipettes is convenient for a wide range of biomedical applications. For high-efficiency cell transportation, the cells must be aspirated into the orifice of a micropipette. However, this is very difficult to achieve, as there is relative movement between the cell and the culture medium when the fluid drives the cell in the culture medium. It is crucial to use cell dynamics rather than fluid dynamics as the control objects to improve control performance and stop the cell immediately when it approaches the micropipette. In this study, the cell dynamics were modeled using a second-order model by integrating the dynamic model between the fluid and the cell into a first-order fluid dynamic model. A backstepping controller-based extended state observer was proposed to control the cell movement inside the micropipette. Experiments demonstrated that the proposed controller could aspirate cells into the orifice of the micropipette with high accuracy and no overshoot. Furthermore, the proposed controller was applied to automated somatic cell nuclear transfer, and it significantly boosted operational efficiency.**

***Note to Practitioners*—The need to apply advanced automation methods to transfer cells in life sciences has increased at a steady pace. The key feature of such systems is the ability to select and transfer cells at a predetermined position in space and time for biological applications. We propose a cell positioning control method based on vision-guided robotics that can directly aspirate cells to specified positions near the orifice of a micropipette. In somatic cell nuclear transfer, the proposed method of transferring somatic cells into oocytes occurs at a faster pace than manual operation. This provides essential functionality for single-cell transfer and is an appropriate technology for practitioners with this functional requirement.**

***Index Terms*—cell transportation, backstepping control, extended state observer, gas pressure compensation.**

This research was jointly supported by National Natural Science Foundation of China (U1813210, 62027812, 62003174). (Corresponding author: Xin Zhao.)

The authors are with the Institute of Robotics and Automatic Information System (IRAIS) and the Tianjin Key Laboratory of Intelligent Robotic (tjKLIR), Nankai University, Tianjin 300350, China, and also with the Institute of Intelligence Technology and Robotic Systems, Shenzhen Research Institute of Nankai University, Shenzhen 518083, China (e-mail: zhaoxin@nankai.edu.cn).

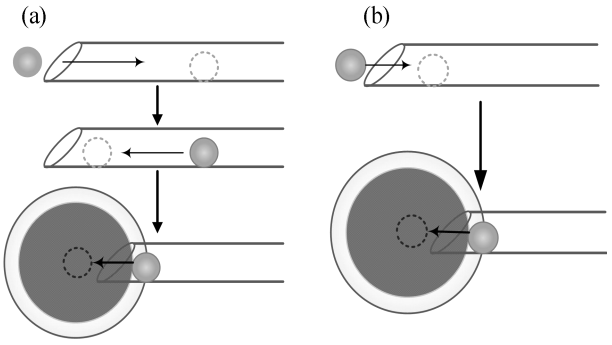

Fig. 1. Cell transfer process. (a) Previous cell transfer. (b) Improved cell transfer.

I. Introduction

Single-cell transportation is one of the most typical cell operations [1]-[6], and numerous successful applications have been demonstrated, including intracytoplasmic sperm injection (ICSI) [7][8], nuclear transfer (animal clone) [7][10], genomic testing [11][12] and preimplantation genetic diagnosis (PGD) [13]-[15]. Micropipettes are the conventional tools used for cell transportation.

Figure 1(a) depicts a typical cell transfer procedure, which involves three steps: 1) aspirating the cell from a Petri dish into the micropipette, 2) positioning the cell in the desired position inside the micropipette, and 3) injecting it out to the target position [16][17]. Some promising results have been obtained in aspirating and positioning cells inside micropipettes [18]-[21]. Ref. [18] proposed a control method to aspirate cells of different sizes and implemented step 1. Ref. [19] proposed a robust controller to position sperm in an ideal position near the orifice of a micropipette in ICSI experiments, implementing step 2.

However, the three-step procedure is not efficient because step 2 (positioning the cell to the desired position inside the micropipette) is not necessary if the cell can be aspirated into the orifice of the micropipette in step 1. Figure 1(b) depicts an improved two-step procedure: 1) aspirating the cell into the micropipette's orifice and 2) injecting it into the target position. Additionally, cell transportation typically requires the transfer of cells to multiple task regions or different types of culture media [22]. However, the culture medium always enters into the micropipette when cells are aspirated. To avoid aspirating excess culture medium into the micropipette and blending different types of culture media, cells should be aspirated into the orifice of the micropipette.

However, aspirating cells into the orifice of a micropipette

is difficult. As Ref. [18] claims, “a relatively large range is needed to guarantee the positioning error to be asymptotic to zero.” A large range typically indicates a longer traveling time and accelerating distance in the subsequent injection step, which results in a cell’s higher traveling speed. Moreover, similar to cell penetration [23], potential cell damage may occur in cell aspiration, since the cell moves at a high speed, a collision occurs between the cell and its new environment. Thus, an additional injection step is necessary after aspirating the cell into the micropipette, i.e., positioning it in the orifice of the micropipette. Therefore, the solution obtained using the integrating method proposed in Refs [18] and [19] is effective in implementing the three-step procedure instead of the high-efficiency cell transportation approach.

In cell aspiration, positioning control begin when the cell approaches the orifice of the micropipette. Cell movement in both the Petri dish and micropipette is driven by the fluid. When being aspirated into the micropipette, the cell accelerates outside the micropipette and decelerates inside the micropipette. There is relative movement between the cell and fluid in the stages of acceleration and deceleration [24]. Therefore, it is necessary to model the cell dynamics rather than the fluid dynamics to stop the cell immediately as it approaches the micropipette.

In this study, a pneumatic system, consisting of a syringe, fluid, and cell, was used to control the movement of cells. A first-order fluid dynamic model was used to describe the interaction between the syringe and fluid. The Stokes viscosity formula was used to describe the interaction between the fluid and the cell. The dynamic model between the fluid and cell was integrated into the first-order fluid dynamic model, and the cell dynamics were modeled as a second-order model. An extended state observer (ESO)-backstepping controller was developed to control cell movement inside the micropipette. Some uncertainties were modeled as disturbances, which were estimated using the ESO and compensated for in the controller [25]. The pressure variance processed using a Kalman filter was also compensated for in the controller to decrease the control error caused by gas hysteresis. Experiments demonstrated that the proposed controller could aspirate cells into the orifice of the micropipette with high accuracy and no overshoot. Furthermore, an experiment on transporting somatic cells into the oocyte using the proposed controller was implemented.

The remainder of this paper is organized as follows: Section II presents the dynamic model of cell aspiration into the micropipette. The cell aspiration and positioning control algorithms are described in Section III. Simulations and experiments with the proposed controller are described in Sections IV and V, respectively. Section VI presents an automated somatic cell nuclear transfer experiment using the proposed control strategy. Finally, Section VII concludes this paper.

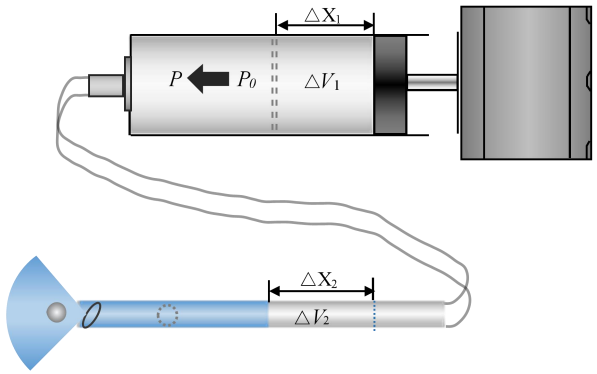

Fig. 2 Schematic of varying pressure inside a micropipette.

II. System Model

In this study, a pneumatic syringe system was used to control cell movement. Stepper motors were used to drive the movement of the piston and plungers inside the syringe, which resulted in varying pressures inside the micropipette. The pressure drove the fluid to flow, then the fluid drove the movement of the cells. The motor speed was taken as the system input, and the cell’s position was the output. In this study, we modeled the cell dynamics by integrating the dynamics of the motor-fluid and fluid-cell.

The following assumptions were adopted to model the cell dynamics inside the micropipette:

1. During cell movement, the ambient temperature remains constant.

2. The catheter is rigid and no shrinking or expansion occurs when aspirating or injecting the cell.

3. The motor and piston are rigidly connected through the lead screw, and no return error occurs.

4. The velocity of the fluid inside the micropipette is relatively constant.

Fluid model inside the micropipette

According to the ideal gas law, the pressure of an ideal gas is inversely proportional to its volume during an isothermal process.

$$P_0 V_0 = PV = C \tag{1}$$

where C is a constant.

Figure 2 shows the schematic of varying pressure inside the micropipette. When the system pressure varies from P_0 to P, the system volume varies from V_0 to V, yielding

$$(V_0 + \Delta V)(P_0 + \Delta P) = P_0 V_0 \tag{2}$$

$$\Delta P = -P_0 \frac{\Delta V}{V_0 + \Delta V} \tag{3}$$

As $V_0 >> \Delta V$, we obtain

$$V_0 + \Delta V \approx V_0 \tag{4}$$

$$\Delta P = -P_0 \frac{\Delta V}{V_0} \tag{5}$$

The volume variation (ΔV) of the closed air inside the system is

$$\Delta V = \Delta V_2 - \Delta V_1 \tag{6}$$

where ΔV_1 is the volume variation of the air inside the syringe, and ΔV_2 is the volume variation of the fluid inside the micropipette:

$$\Delta V_1 = \Delta x_1 A_1 \tag{7}$$

$$\Delta V_2 = \Delta x_2 A_2 \tag{8}$$

where A_1 and A_2 are the sectional areas of the syringe and micropipette, respectively, Δx_1 and Δx_2 are the position changes of the piston and gas-liquid interface (GLI), respectively. Substituting (7) and (8) into (6) yields

$$\Delta V = \Delta x_2 A_2 - \Delta x_1 A_1 \tag{9}$$

Substituting (9) into (5) yields

$$\Delta P = -P_0 \frac{\Delta x_2 A_2 - \Delta x_1 A_1}{V_0} \tag{10}$$

Differentiating both sides of equation (10), we obtain

$$\dot{P} = \frac{P_0}{V_0}(\dot{x}_1 A_1 - \dot{x}_2 A_2) \tag{11}$$

where $\dot{x}_1 = u$ denotes the speed of the motor:

$$\dot{x}_2 + \frac{V_0}{P_0 A_2}\dot{P} = \frac{A_1}{A_2}u \tag{12}$$

The system model is

$$\begin{cases} \dot{x}_2 = \dfrac{A_1}{A_2}u - \dfrac{V_0}{P_0 A_2}\dot{P} \\ y = x_2 \end{cases} \tag{13}$$

Cell dynamic model inside the micropipette

When a cell moves in a fluidic environment, it suffers from a hydrodynamic drag force [26]–[28], the drag force exerted on the cell is

$$F_d = 6\pi\mu r(v_l - v_c) \tag{14}$$

where v_l and v_c denote the fluid speed and cell speed, respectively, μ is the dynamic viscosity, and r is the radius of the cell.

According to Newton's law, the dynamic model of the cell in the fluid is

$$\frac{m}{6\pi\mu r}\ddot{x}_c = v_l - v_c \tag{15}$$

where m denotes the mass of the cell.

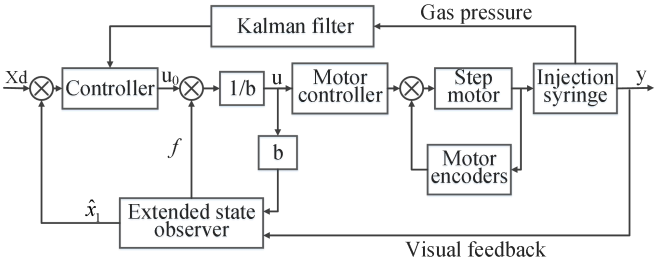

Fig. 3. Control architecture of cell movement.

Let $v_l = \dot{x}_2$; substituting (15) into (13), we obtain

$$\frac{m}{6\pi\mu r}\ddot{x}_c + \dot{x}_c = \frac{A_1}{A_2}u - \frac{V_0}{P_0 A_2}\dot{P} \tag{16}$$

The cell dynamic model is

$$\begin{cases} \dot{x}_{c1} = x_{c2} \\ \dot{x}_{c2} = -\theta_1 x_{c2} - \theta_1\theta_2\dot{P} + b\theta_1 u + f \end{cases} \tag{17}$$

where $b = A_1/A_2$, $\theta_1 = 6\pi\mu r/m$, and $\theta_2 = V_0/P_0 A_2$. The perturbation term $f(\cdot)$ denotes the lumped uncertainties, including the hysteresis effect of the closed air pressure, model parameter uncertainties, unmodeled dynamics, and other disturbances.

III. Cell Movement Control Inside the Micropipette

Figure 3 shows the control architecture of the cell movement. The positions of the cell were taken as the control output, and the positions of the cell and micropipette were obtained online using visual tracking algorithms. The gas pressure inside the micropipette as a state variable was collected using a sensor and processed using the Kalman filter. Meanwhile, the ESO was used to observe the system states and estimate the lumped disturbance.

A. State Observer Design

The state-space model of cell movement is represented in (17). We set $f(\cdot) = x_{c3}$, representing the lumped uncertainties. The key of the control system is to estimate the lumped uncertainties $f(\cdot)$ using the ESO. The system was updated online by measuring the input and output states, and a lumped disturbance was estimated for the high accuracy of the system model.

A linear extended state observer was designed to estimate the state variables:

$$\dot{\hat{x}}_1 = \hat{x}_2 - \beta_1(\hat{x}_1 - y) \tag{18a}$$

$$\dot{\hat{x}}_2 = \hat{x}_3 - \beta_2(\hat{x}_1 - y) + b_0 u \tag{18b}$$

$$\dot{\hat{x}}_3 = -\beta_3(\hat{x}_1 - y) \tag{18c}$$

where $\hat{\boldsymbol{x}} = [\hat{x}_1, \hat{x}_2, \hat{x}_3]^T$ is the estimation for $\boldsymbol{x}_c = [x_{c1}, x_{c2}, x_{c3}]^T$, and y denotes the control system output, namely, cell position x_c.

We define $\tilde{x}_i = x_{ci} - \hat{x}_i$ as the estimation error of the ESO, and the estimation error is

$$\dot{\tilde{x}}_1 = -\beta_1 \tilde{x}_1 + \tilde{x}_2 \tag{19a}$$

$$\dot{\tilde{x}}_2 = -\beta_2 \tilde{x}_1 + \tilde{x}_3 \tag{19b}$$

$$\dot{\tilde{x}}_3 = -\beta_3 \tilde{x}_1 + f(\cdot) \tag{19c}$$

The characteristic polynomial of the linear ESO (LESO) is

$$\lambda(s) = s^3 + \beta_1 s^2 + \beta_2 s + \beta_3 \tag{20}$$

Ref. [25] proposed a simple method to determine the parameters in designing a LESO based on the bandwidth of the observer, w_0. With $\beta_1 = 3w_0$, $\beta_2 = 3w_0^2$, and $\beta_3 = w_0^3$, the characteristic polynomial of the LESO is set as $(s + w_0)^3$ such that the characteristic polynomial is a Hurwitz polynomial.

The total control law u is a combination of the designed control signal u_0 and the disturbance compensation $\hat{x}_3$. It can be expressed as

$$u = \frac{u_0 - \hat{x}_3}{b}. \tag{21}$$

Theorem 1: Assuming that $\dot{f}$ is bounded, there exists a positive constant $\varepsilon_i > 0$ and a finite time $T_1 > 0$, the estimated error $|\tilde{x}_i(t)| \le \varepsilon_i$, $i = 1,2,3$, $\forall t > T_1 > 0$ and $w_0 > 0$.

Proof: See Appendix A.

Assumption 1: According to (17), we assume that $f(t)$ is bounded. There exists a positive constant h_1 such that $f(t) < h_1$.

B. Controller Design

The cell position error of the closed-loop control system is defined as

$$e_1 = x_{c1} - x_{1d} \tag{22}$$

where x_{c1} is the cell position inside the micropipette, and x_{1d} denotes the desired trajectory.

We define a Lyapunov function candidate as follows

$$V_1 = \frac{1}{2} e_1^2 \tag{23}$$

Considering (17) and (22) and differentiating (23) with respect to time, we obtain

$$\dot{V}_1 = e_1 \dot{e}_1 = e_1 (x_{c2} - \dot{x}_{1d}) \tag{24}$$

To guarantee $\dot{V}_1$ is negative definite, a virtual control variable is introduced as follows:

$$x_{2d} = \dot{x}_{1d} - k e_1 \tag{25}$$

where k is a positive constant.

We define

$$e_2 = x_{c2} - x_{2d} \tag{26}$$

We define a Lyapunov function candidate as follows:

$$V_2 = V_1 + \frac{1}{2} e_2^2 \tag{27}$$

Differentiating (27) with respect to time yields

$$\begin{aligned} \dot{V}_2 &= e_1 e_2 - k e_1^2 + e_2 \dot{e}_2 \\ &= e_1 e_2 - k e_1^2 + k \dot{e}_1 e_2 - e_2 \ddot{x}_{1d} - \theta_1 e_2 x_{c2} \\ &\quad - \theta_1 \theta_2 e_2 \dot{p} + e_2 b_0 \theta_1 u + e_2 f \end{aligned} \tag{28}$$

The controller is designed as follows:

$$u = \frac{1}{b_0 \theta_1} \left(-e_1 - k\dot{e}_1 + \ddot{x}_{1d} + \theta_1 x_{c2} + \theta_1 \theta_2 \dot{p} - k e_2 - \beta \frac{\frac{e_2}{\theta}}{\left| \frac{e_2}{\theta} + \alpha \right|} - \hat{x}_3 \right) \tag{29}$$

where $\varphi(e_2) = \frac{e_2}{\theta} \Big/ \left| \frac{e_2}{\theta} + \alpha \right|$, parameters θ and α satisfy positive constants, and β is the upper bound of the observation error of the disturbance, that is, $\beta \ge \varepsilon_3$.

Theorem 2: With the ESO accurately estimating the disturbance, $|f - \hat{x}_3| < \varepsilon_3$, the equilibrium is uniformly stable in the closed-loop control system under the backstepping controller (29). That is, $|e| < \varepsilon$ as time $t \to 0$.

Proof: See Appendix B.

C. Gas Pressure Estimation using the Kalman Filter

To obtain a smooth signal, the Kalman filter is used to process the measured gas pressure from the noisy sensor output, which is the feedback in the control system.

Step 1: Given $x(k-1|k-1)$ and $P(k-1|k-1)$, the state prediction is executed as

$$\hat{x}(k|k-1) = F(k)\hat{x}(k-1|k-1) + B(k)u(k-1) \tag{30}$$

$$P(k|k-1) = \mathrm{F}(k)P(k-1|k-1)F(k)^T + GQG^T. \tag{31}$$

Step 2: After obtaining the new measurement, $Y(k)$, the following measurement update is conducted:

$$\hat{x}(k|k) = \hat{x}(k|k-1) + K(k)\tilde{y}(k) \tag{32}$$

$$P(k|k) = (I - K(k)C)P(k|k-1) \tag{33}$$

where P is the covariance of mean value, $K(k)$ is the Kalman gain, and $\tilde{y}(k)$ is the measurement residual

$$K = \frac{P(k|k-1)C^T}{CP(k|k-1)C^T + R} \tag{34}$$

$$\tilde{y}_k = Y(k) - C\hat{x}(k|k-1) \tag{35}$$

With the optimized gas pressure $\hat{x}(k|k)$, the rate of change in gas pressure and the feedback into the controller as a compensation item are calculated. The variance of the gas pressure is a component of the lumped uncertainties, and the compensation item is obtained to lower the lumped uncertainties. Thus, ESO can play a better role in estimating uncertainties.

IV. Simulations

Simulations were performed to verify the effectiveness of the proposed method. The model and controller were built

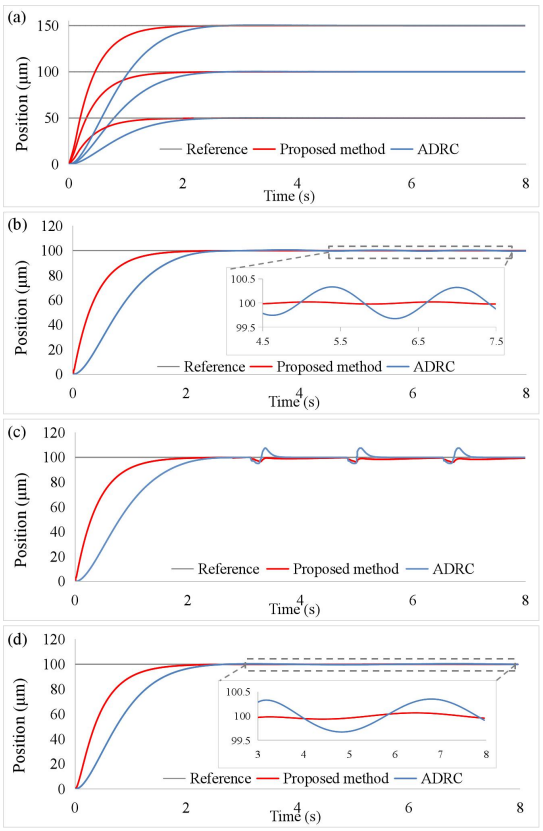

Fig. 4. Simulation results of step control. (a) Simulation results with different distances. (b) System steady position result with model uncertainty. (c) System control performance with external disturbance. (d) System steady position result with model parameter varying.

TABLE I: System parameters for simulation

Symbol	Value	Symbol	Value
b	100	∂	0.03
θ_1	1	β	0.021
θ_2	1	k	2.2
θ	0.11	ω_0	100

using MATLAB/Simulink. The sampling time of the system was set to 10 ms. The model parameters and proposed gain controller are listed in Table I. The proposed controller was compared with the active disturbance rejection controller (ADRC), in which the control gains were set as ω_c = 4.8 and ω_0 = 100.

Step response testing was conducted to verify the transient response performance of the proposed controller. Figure 4(a) shows the simulation results for different step distances (50 μm, 100 μm, 150 μm). The simulation results indicate that both the proposed controller and ADRC could converge to the target position and remain stable. However, the performance of the proposed controller was superior to that of the classic ADRC in terms of settling time: 2.25 s Vs. 2.54 s for distance 50 μm, 2.03 s Vs. 2.47 s for distance 100 μm, 1.76 s Vs. 2.18 s for distance 150 μm.

The internal uncertain factors originated from the model inaccuracy in the dynamics equation. The simulation results

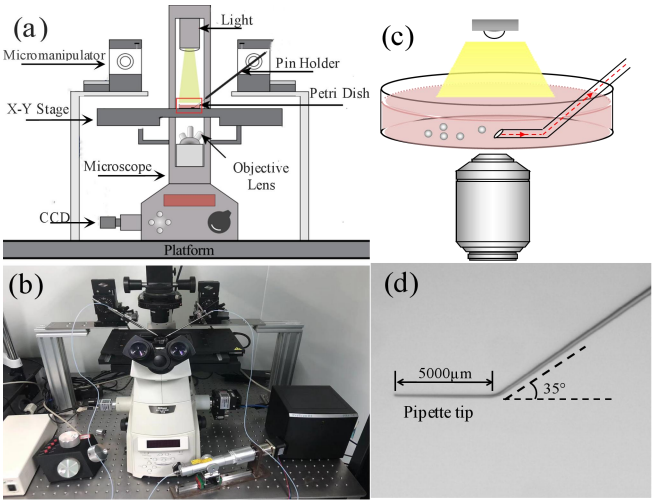

Fig. 5. Cell micro-manipulation system for experiment. (a) System schematic diagram. (b) System setup. (c) Aspirating cell schematic diagram. (d) Micropipette.

with model uncertainty $f(t)$ as a sinusoidal function y=10sin(3.14t) μm are shown in Figure 4(b). The stable state for the position error with the proposed controller had smaller fluctuations than that with the ADRC (0.08 μm vs. 0.25 μm). External disturbances primarily resulted from the vibration of the X-Y stage and the catheter being touched. Figure 4(c) depicts the performance of the two controllers when a pulse signal is treated as an external disturbance. The simulation results demonstrated that the proposed controller generated smaller response fluctuations than the ADRC (3.7 μm vs. 8.1 μm) as it provided effective control with small stable state position errors. In addition, the viscosity of the culture medium may have fluctuated with temperature and other factors, causing changes in the model parameters. Figure 4 (d) shows the simulation results when the parameter θ_1 was a sinusoidal function of 0.5sin(0.5t) μm. In the absence of dynamic uncertainty and external disturbances, the proposed method performed better in terms of robustness and disturbance rejection.

V. Experimental Results

Polystyrene microbeads (diameter = 15 μm, density = 1.05 g/cm^3) were used in the experiment first to maintain the consistency of the experimental conditions. Subsequently, the two types of cells with different diameters were aspirated into a micropipette in the experiments. The microbeads or cells were dispensed in a Petri dish filled with the culture medium. The tip of the micropipette was placed horizontally at the bottom of the Petri dish, facilitating object aspiration.

A. System Setup

Experiments were performed using NK-MR901, as shown in Figure 5. The setup was built based on a standard inverted microscope (Nikon, Eclipse TI-E, Japan) with a CCD (Balser, acA645-100gm, Germany). The CCD was used to gather microscopic images with a resolution of 640×480 pixels and a frame rate of 50 frame/s. A motorized X-Y stage (ProScan III,

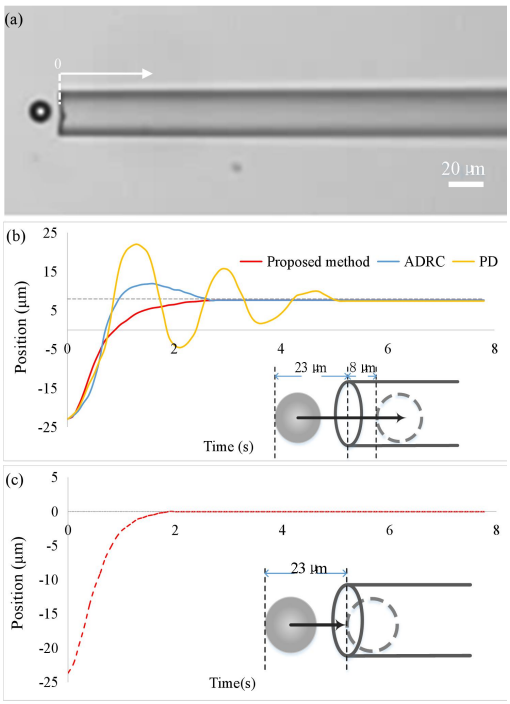

Fig. 6. Aspirating microbead to orifice. (a) Microbead initial state before aspirating. (b) Control result for aspirating microbead into orifice. (c) Control result for aspirating microbead to orifice.

TABLE II: System parameters for experiment

Symbol	Aspirating microbead	Aspirating cell	Aspirating oocyte
b	2000	890	28
θ_1	8	5	2
θ_2	2.5	1.2	0.34
θ	2.6	2.6	3.4
∂	0.55	0.65	1.2
β	0.32	0.32	0.61
k	4.5	4	4.1
ω_0	15	15	18

Prior, motion range: 120 mm×80 mm, positioning resolution: 0.05 μm) was used to hold the Petri dish containing the culture medium. A pair of X-Y-Z micromanipulators (MP285, Sutter, motion range: 25 mm, positioning resolution: 0.04 μm) was used for mounting micropipettes, and a host computer was used for microscopic image processing and motion control of the stage and manipulators. A pneumatic syringe (Narishige, IM-11B, Japan) was connected to the micropipette through a catheter; a step motor (Sanyo, 103H546-0410, Japan) was connected to the lead screw of the pneumatic syringe through a coupling, and a syringe motor controller (Vince, VSMD101_025T, China) was used to drive the step motor. Gas pressure was measured using a sensor (Honeywell, HSCSDRN400MDAA3, USA). I/O modules (ALD, CC2530, China) were connected to the gas pressure sensor to acquire the sensor signal and transmit it to the control system.

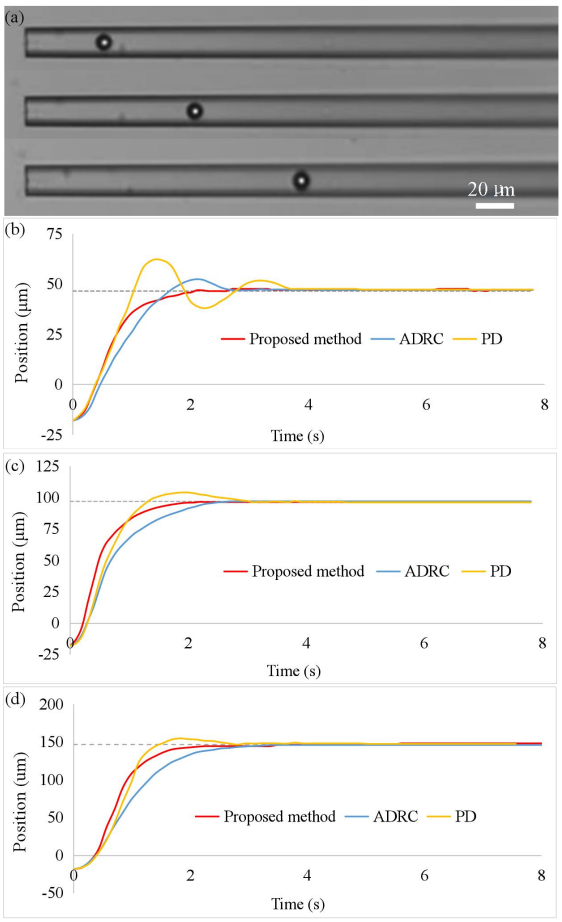

Fig. 7. Aspirating microbead control experiment. (a) Aspirating microbead into micropipette. (b) Control result for aspirating microbead into micropipette 50 μm. (c) Control result for aspirating microbead into micropipette 100 μm. (d) Control result for aspirating microbead into micropipette 150 μm.

B. Aspirating Microbead into the Orifice of a Micropipette

It is necessary to aspirate microbeads into the orifice of a micropipette for transportation applications, which facilitates the transfer of microbeads to the desired position in subsequent operations. The microbead was initially located outside the micropipette, and the orifice of the micropipette was set as the origin (Figure 6(a)). The GLI of the micropipette was placed at a specific position to ensure the consistency of the performance. In order to prevent the movement of the GLI from affecting the visual tracking of the microbeads, the GLI was placed outside the field of view of the microscope.

First, experiments to aspirate the microbeads into the micropipette were performed. The model parameters and gains of the proposed controller are listed in Table II. For comparison, the parameters of ADRC were set as ω_c =5.2 and ω_0 =12.4, and the parameters of a proportional-derivative (PD) controller were set as k_p =7.4 and k_d =3.1. Figure 6(b) depicts the experimental results of aspirating the microbead from the outside to a target position near the orifice inside the micropipette. The proposed method could position the microbead to the target position with a settling time of 2.23 s and no overshoot, whereas the experimental results with the

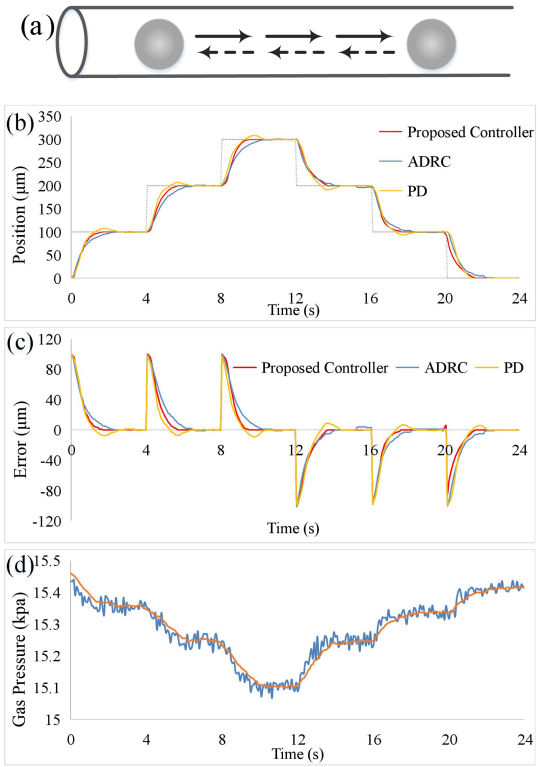

Fig. 8. Cell step control with 100 μm. (a) Cell movement control inside micropipette. (b) Step control results. (c) Tracking errors with different controllers. (d) Changing of gas pressure in system..

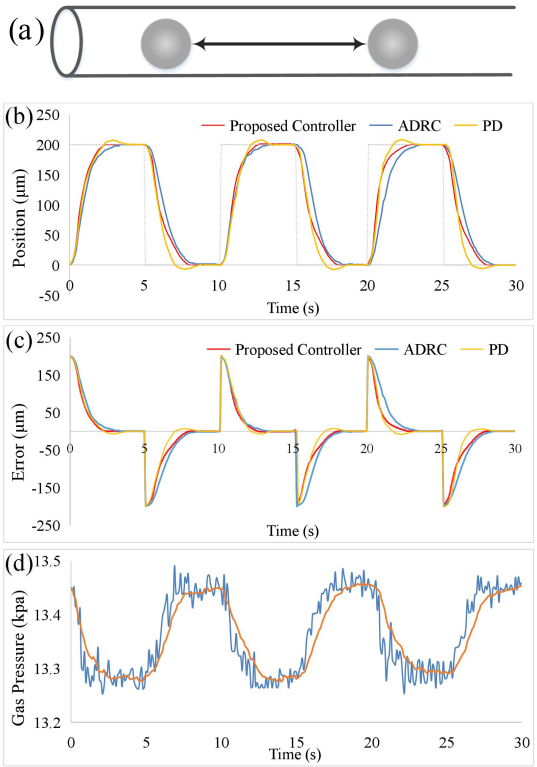

Fig. 9. Cell step control with 200 μm. (a) Cell movement control inside micropipette. (b) Step control results. (c) Tracking errors with different controllers. (d) Changing of gas pressure in the system..

ADRC had a larger settling time and overshoot; the PD controller generated a large oscillation (37.7%) and had a much longer settling time (4.88 s). Large oscillations may result in the microbead falling outside the micropipette, and a long settling time results in low operation efficiency. The experiments with the proposed controller exhibited higher stability and a smaller response time.

To explore the limit position near the orifice inside the micropipette, the proposed controller was used to position the microbead at the original point, which would indicate that the microbead stopped immediately when it crossed the orifice of the micropipette. Figure 6(c) shows that the microbead successfully stopped at the orifice of the micropipette without overshoot by using the proposed controller. However, the microbeads with the PD controller and ADRC remained stuck outside the orifice and could not be successfully aspirated into the micropipette.

Figure 7 shows the experiments of aspirating the microbead into the micropipette away from the orifice. Figure 7(b) shows the experimental results with a target position of 50 μm from the orifice. Compared with the ADRC and PD controllers, the proposed controller could position the microbead to the desired position inside the micropipette with a smaller settling time (2.12 s), while the settling times for the ADRC and PD controllers were 2.76 and 3.84 s, respectively. In addition, the proposed controller did not produce an overshoot. A larger overshoot may result in the disappearance of the microbead in the field of view and failure of microbead aspiration. Figure 7(c) shows the control results with a target position of 100 μm from the orifice. Compared with the ADRC and PD controllers, the proposed controller demonstrated a smaller settling time. The proposed controller and ADRC did not generate an overshoot, whereas the PD controller produced a 7.2% overshoot. Figure 7(d) shows the control results with a target position of 150 μm from the orifice. The proposed controller also had a shorter settling time (2.18 s) than the ADRC (3.15 s) and PD controller (3.32 s), whereas the proposed controller and ADRC did not generate an overshoot, and the PD controller produced a 3.5% overshoot.

Aspirating the microbead into the orifice of the micropipette is difficult because more disturbances and uncertainties occur when the microbead crosses the orifice. Compared with the ADRC and PD controllers, the proposed controller can aspirate the microbead from the outside to any position inside the micropipette, even at the orifice, with faster response and no overshoot. Experiments with the PD controller typically had a large overshoot and settling time, as it had no model and compensation items. Furthermore, the proposed controller outperformed the standard ADRC because the fluctuation in gas pressure is treated as compensation and adjusted for in the proposed controller.

C. Positioning a Microbead Inside the Micropipette

Experiments on microbead step control inside the micropipette were conducted to further verify the dynamic performance of the proposed controller. The microbeads were initially placed inside the micropipette, and then controlled to

move forward and backward inside the micropipette in steps of 100 and 200 μm, respectively.

To compare the control performance quantitatively with different controllers, the average overshoot (AOS) and average settling time (AST) were defined as follows:

$$AOS = \frac{\sum_{k=1}^{N}\left[x_{ok}(t_p) - x_{ok}(\infty)\right] \Big/ x_{ok}(\infty)}{N} \tag{36}$$

$$AST = \frac{\sum_{k=1}^{N} t_s(k)}{N} \tag{37}$$

where N is the total number of the step controls.

The experimental results are shown in Figs. 8 and 9. The performances of the different controllers are summarized in Table III. The experimental results with the proposed controller and ADRC exhibited no overshoot. The PD controller produced AOSs of 6.53% and 3.25% with steps of 100 and 200 μm, respectively. The proposed controller had a faster response than the ADRC and PD controllers in both the 100 and 200 μm step controls, and the ADRC had a faster response than the PD controller. The ASTs with the proposed controller, ADRC, and PD controller in the step control of 100 μm were 2.13, 2.65, and 2.82 s respectively. The ASTs with the proposed controller, ADRC, and PD controller in the 200 μm step control were 2.42, 3.34, and 3.63 s, respectively. Figures 8(d) and 9(d) show the variation in the gas pressure in the system, with the blue line denoting the measured gas pressure and the red line denoting the filtered gas pressure using Kalman filtering.

In summary, the experimental results demonstrated that the proposed controller accurately positions the microbead at any position inside the micropipette with faster response and smaller settling time than the ADRC and PD controllers.

TABLE III: Performance Comparison

Distance	Performance	Proposed	ADRC	PD
100 μm	AOS (s)	2.13	2.65	2.82
	AST (%)	N	N	6.53
200 μm	AOS (s)	2.42	3.34	3.63
	AST (%)	N	N	3.25

D. Aspirating Cells into Micropipettes

Experiments on aspirating somatic cells (porcine fetal fibroblasts) and porcine oocytes to target positions inside the micropipette were conducted to verify the performance of the proposed controller. Figure 10(a) shows the somatic cell and micropipette; the diameters of the somatic cell and micropipette were 25 and 30 μm, respectively. Figure 10(b) shows the oocyte and micropipette, whose diameters were 150 and 170 μm, respectively. Figure 10(c) shows the control results of aspirating somatic cells at positions 13 (half of the somatic cell diameter), 50, and 100 μm away from the orifice inside the micropipette, respectively. The experimental results with the proposed controller exhibited no overshoot and short settling time of 3.84, 4.03, and 4.22 s, respectively. Figure 10(d) shows the control results of aspirating the porcine

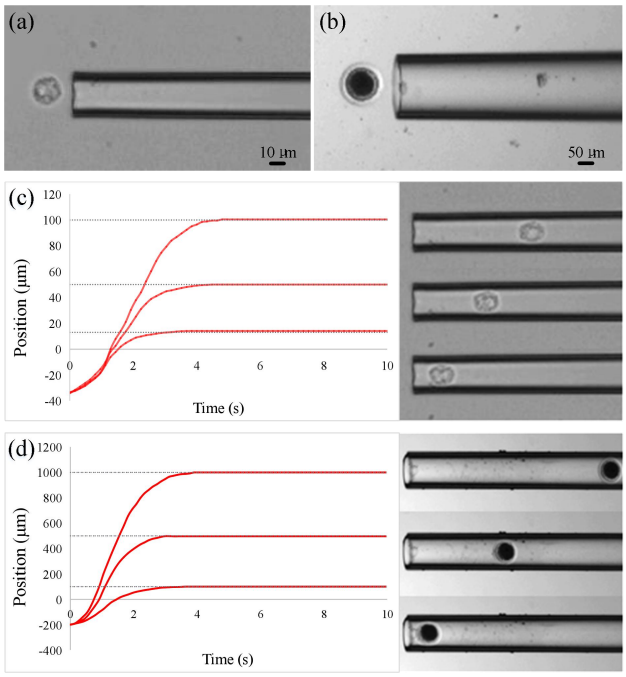

Fig. 10. Aspirating cell control results. (a) Aspirating somatic cell with 25 μm diameter. (b) Aspirating porcine oocyte with 150 μm diameter. (c) Control result for aspirating somatic cell. (d) Control result for aspirating oocyte.

oocyte with step distances of 80 (half of the oocyte diameter), 500, and 1000 μm away from the orifice inside the micropipette. The experimental results with the proposed controller also indicated no overshoot and short settling time of 3.22, 3.51, and 3.88 s, respectively. The proposed controller could aspirate the cells into a position near half of the cell diameter from the orifice, verifying its good performance.

VI. Automated Somatic Cell Nuclear Transfer Application

The proposed control strategy was applied to automated somatic cell nuclear transfer. Figures 11 and 12 show the flowchart and process of the automated somatic cell nuclear transfer based on the proposed controller.

Initially, the somatic cells were placed at the bottom of the Petri dish, and the micropipette was far away from the cells. First, the positions of the target somatic cell and the micropipette were detected using image processing. Second, the micropipette moved to the target cell, guided by a planned path [16]. Third, the target cell was aspirated into the micropipette at a position near the orifice using the proposed controller. Finally, the micropipette penetrated the oocyte, and then the somatic cell was injected into the oocyte.

The experimental results showed that the average time of transferring one cell, from cell detection to cell injection, was 25 s. The proposed controller facilitates the two-step cell transfer procedure (skipping the positioning cell inside the micropipette), and the operation time was decreased by 20 s compared with the manual operation. The proposed controller was successfully applied in somatic cell nuclear transfer and significantly increased the operating efficiency.

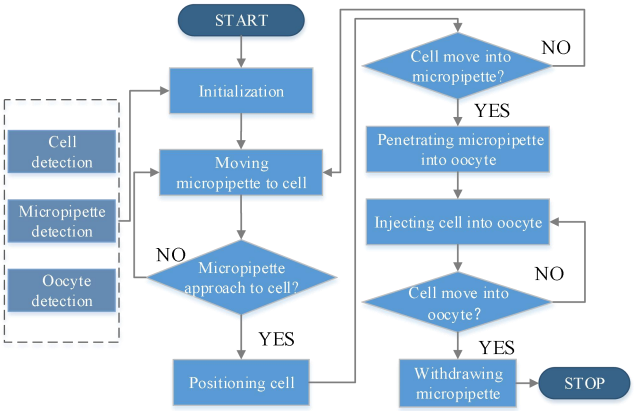

Fig. 11. Flowchart of the automated somatic cell transfer operation.

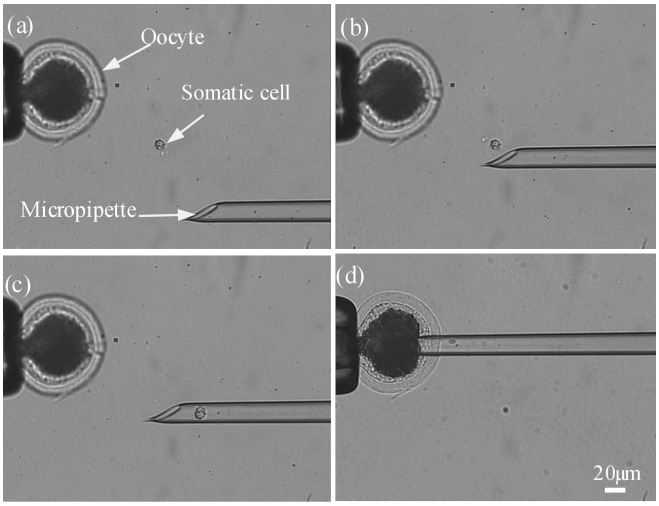

Fig. 12. Process of automated somatic cell nuclear transfer. (a) Visual detection of the somatic cell, oocyte and micropipette. (b) Moving the micropipette to approach to the target somatic cell. (c) Aspirating the cell into the micropipette and positioning it to the target position. (d) Penetrating the enucleated oocyte using the micropipette and injecting the somatic cell into the oocyte.

VII. Conclusion

Single-cell transportation is one of the most common cell operations. The essential step is to aspirate the cell into the orifice of the micropipette for high efficiency. Therefore, it is crucial to model the dynamics of cell movements in fluids. In this study, the cell dynamics was modeled as a second-order model by integrating the dynamic model between the fluid and cell into a first-order fluid dynamic model. Subsequently, a backstepping controller-based extended state observer was developed to control cell movement inside the micropipette. Experiments showed that the proposed controller aspirated cells into the orifice of the micropipette with high accuracy and no overshoot. Moreover, the simulation and experimental results indicated that the proposed controller aspirated and positioned the microbeads and cells of different sizes to the target position inside the micropipette with short settling time and no overshoot. Furthermore, the proposed controller was successfully applied in automated somatic cell nuclear transfer with an average time of 25 s (vs. 45 s manually), which significantly increased the operating efficiency.

Appendix 1:

We define $\eta_i = \frac{\tilde{x}_i}{\omega_0^{\,i}} (i = 1,2,3)$; thus, equation (19) can be rewritten as

$$\dot{\boldsymbol{\eta}} = \omega_0 A_\eta \boldsymbol{\eta} + B_\eta \frac{f}{\omega_0^{\,3}}, \tag{36}$$

where $A_\eta = \begin{bmatrix} -3 & 1 & 0 \\ -3 & 0 & 1 \\ -1 & 0 & 0 \end{bmatrix}$, $B_\eta = \begin{bmatrix} 0 \\ 0 \\ 1 \end{bmatrix}$.

Because A_η satisfies a Hurwitz polynomial for $\forall \omega_0 > 0$, a Lyapunov function is defined as $V(\eta) = \eta^T P_\eta \eta$, where P_η is a positive definite symmetric matrix that satisfies $A_\eta^{\,T} P_\eta + P_\eta A_\eta = -Q_\eta$.

The time derivative of $V(\eta)$ is

$$\begin{aligned} \dot{V}(\eta) &= -\omega_0 \eta^T Q_\eta \eta + 2\eta^T P_\eta B_\eta \frac{h}{\omega_0^{\,3}} \\ &\le -\omega_0 \lambda_{\min}(Q_\eta) \|\eta\|^2 + \frac{2L_h \lambda_{\max}(P_\eta) \|\eta\|}{\omega_0^{\,3}} \end{aligned} \tag{37}$$

For $V(\eta)$ satisfying $\lambda_{\min}(P_\eta)\|\eta\|^2 \le V(\eta) \le \lambda_{\max}(P_\eta)\|\eta\|^2$, that is $\frac{V(\eta)}{\lambda_{\max}(P_\eta)} \le \|\eta\|^2 \le \frac{V(\eta)}{\lambda_{\min}(P_\eta)}$; substituting it into (37) yields

$$\dot{V}(\eta) \le -\omega_0 \frac{\lambda_{\min}(Q_\eta)}{\lambda_{\max}(P_\eta)} V(\eta) + \frac{2L_h \lambda_{\max}(P_\eta)}{\omega_0^{\,3} \sqrt{\lambda_{\min}(P_\eta)}} \sqrt{V(\eta)} \tag{38}$$

We define $W = \sqrt{V(\eta)}$, we obtain $\dot{W} = \frac{\dot{V}(\eta)}{2\sqrt{V(\eta)}}$; substituting it into (38) yields

$$\dot{W} \le -\omega_0 \frac{\lambda_{\min}(Q_\eta)}{2\lambda_{\max}(P_\eta)} W + \frac{L_h \lambda_{\max}(P_\eta)}{\omega_0^{\,3} \sqrt{\lambda_{\min}(P_\eta)}} \tag{39}$$

Applying the Gronwall–Bellman inequality for (39) yields

$$\begin{aligned} \dot{W} \le -\Big(\frac{2L_h \lambda^2_{\max}(P_\eta)}{\omega_0^{\,4} \lambda_{\min}(Q_\eta) \sqrt{\lambda_{\min}(P_\eta)}} - W(t_0)\Big) e^{-\omega_0 \frac{\lambda_{\min}(Q_\eta)}{2\lambda_{\max}(P_\eta)}(t-t_0)} \\ + \frac{2L_h \lambda_{\max}{}^2(P_\eta)}{\omega_0^{\,4} \lambda_{\min}(Q_\eta) \sqrt{\lambda_{\min}(P_\eta)}} \end{aligned} \tag{40}$$

With $t \to \infty$, $\|\eta\|$ satisfies

$$\|\eta\| \le \frac{\sqrt{V}}{\sqrt{\lambda_{\min}(P_\eta)}} \le \frac{2L_h \lambda_{\max}{}^2(P_\eta)}{\omega_0^{\,4} \lambda_{\min}(P_\eta) \lambda_{\min}(Q_\eta)} = \frac{M_e}{\omega_0^{\,4}} \tag{41}$$

where $M_e = \frac{2L_h \lambda_{\max}{}^2(P_\eta)}{\lambda_{\min}(P_\eta)\lambda_{\min}(Q_\eta)}$ is a positive constant.

Because P_η and Q_η are independent of ω_0, using (41), we obtain

$$\lim_{\omega_0 \to \infty, t \to \infty} \|\eta\| = 0 \tag{42}$$

With $\eta_i = \frac{e_i}{\omega_0^{\,i}} (i = 1,2,3)$, we obtain $\lim_{\omega_0 \to \infty, t \to \infty} \|e\| = 0$. Therefore, the observation error of the LESO can be reduced by increasing the value, and the observation error can be maintained within a very small range.

Appendix 2:

Lemma: For all $z \in R$, $\theta > 0$, $\alpha > 0$, that is

$$|z| - z\frac{\frac{z}{\theta}}{\left|\frac{z}{\theta}\right| + \alpha} < \theta\alpha \tag{43}$$

Proof

Case 1: $z > 0$,

$$|z| - z\frac{\frac{z}{\theta}}{\left|\frac{z}{\theta}\right| + \alpha} = z - z\frac{\frac{z}{\theta}}{\frac{z}{\theta} + \alpha} = \frac{z\theta\alpha}{z + \theta\alpha} < \theta\alpha. \tag{44}$$

Case 2: $z = 0$,

$$|z| - z\frac{\frac{z}{\theta}}{\left|\frac{z}{\theta}\right| + \alpha} = 0 < \theta\alpha. \tag{45}$$

Case 3: $z < 0$,

$$|z| - z\frac{\frac{z}{\theta}}{\left|\frac{z}{\theta}\right| + \alpha} = -z - z\frac{\frac{z}{\theta}}{-\frac{z}{\theta} + \alpha} = \frac{-z\theta\alpha}{-z + \theta\alpha} < \theta\alpha. \tag{46}$$

holds.

Controller Stability Proof

Substituting (29) into (28) yields:

$$\begin{aligned} \dot{V}_2 &= \dot{V}_1 + \frac{1}{2}e_2{}^2 \\ &= -ke_1{}^2 - ke_2{}^2 + e_2(f - \hat{x}_3) - e_2\beta\frac{\frac{e_2}{\theta}}{\left|\frac{e_2}{\theta} + \alpha\right|} \end{aligned} \tag{47}$$

Because $|x_{c3} - \hat{x}_3| \le \varepsilon_3$, with $\beta \ge \varepsilon_3$, we obtain

$$\begin{aligned} &|x_{c3} - \hat{x}_3| \le \beta \\ &\Rightarrow e_2(x_{c3} - \hat{x}_3) \le \beta|e_2| \\ &\Rightarrow e_2(x_{c3} - \hat{x}_3) - e_2\beta\sigma(e_2) \le \beta|e_2| - e_2\beta\sigma(e_2) \end{aligned} \tag{48}$$

From the lemma, we observe that

$$|e_2| - e_2\sigma(e_2) < \theta\alpha \tag{49}$$

Therefore,

$$\begin{aligned} &\beta|e_2| - e_2\beta\sigma(e_2) < \beta\theta\alpha \\ &\Rightarrow e_2(x_{c3} - \hat{x}_3) - e_2\beta\sigma(e_2) < \beta\theta\alpha \end{aligned} \tag{50}$$

$\dot{V}_2$ satisfies

$$\begin{aligned} \dot{V}_2 &= -ke_1{}^2 - ke_2{}^2 + e_2(x_{c3} - \hat{x}_3) - e_2\beta\frac{\frac{e_2}{\theta}}{\left|\frac{e_2}{\theta}\right| + \alpha} \\ &< -ke_1{}^2 - ke_2{}^2 + \beta\theta\alpha \end{aligned} \tag{51}$$

Substituting (23) and (27) into (51) yields

$$\dot{V}_2 = -kV_2 + \beta\theta\alpha \tag{52}$$

Solving (52) yields

$$V_2(t) < e^{-k(t-T_1)}V_2(T_1) + \frac{\beta\theta\alpha}{k}(1 - e^{-k(t-T_1)}) \tag{53}$$

$$\Rightarrow \frac{1}{2}e_1{}^2 < e^{-k(t-T_1)}V_2(T_1) + \frac{\beta\theta\alpha}{k}(1 - e^{-k(t-T_1)}) \tag{54}$$

$$\Rightarrow e_1 \le \sqrt{2e^{-k(t-T_1)}V_2(T_1) + \frac{2\beta\theta\alpha}{k}(1 - e^{-k(t-T_1)})} \tag{55}$$

$$\Rightarrow \lim_{t\to\infty} e_1 \le \sqrt{\frac{2\beta\theta\alpha}{k}} \tag{56}$$

Therefore, the position error e_1 is ultimately bounded, and the bounds can be maintained within a very small range using the control parameters k, β, and θ.

REFERENCES

[1] M. Xie, X. Li, Y. Wang, Y. Liu and D. Sun, "Saturated PID Control for the Optical Manipulation of Biological Cells," IEEE Transactions on Control Systems Technology, vol. 26, no. 5, pp. 1909-1916, Sept. 2018.

[2] Z. Chi, Q. Xu and L. Zhu, "A Review of Recent Advances in Robotic Cell Microinjection," IEEE Access, vol. 8, pp. 8520-8532, 2020.

[3] J. Liu, V. Siragam, Z. Gong, J. Chen, M. D. Fridman, C. Leung, Z. Lu, C. Ru, S. Xie, and J. Luo, " Robotic adherent cell injection for characterizing cell – cell communication, " IEEE Transactions on Biomedical Engineering, vol. 62, no. 1, pp. 119-125, 2014.

[4] M. Xie, A. Shakoor, Z. Wu and B. Jiang, "Optical Manipulation of Biological Cells With a Robot-Tweezers System: A Stochastic Control Approach," IEEE Transactions on Circuits and Systems II: Express Briefs, vol. 67, no. 12, pp. 3232-3236, Dec. 2020.

[5] M. Xie, J. K. Mills, Y. Wang, M. Mahmoodi and D. Sun, "Automated Translational and Rotational Control of Biological Cells With a Robot-Aided Optical Tweezers Manipulation System," IEEE Transactions on Automation Science and Engineering, vol. 13, no. 2, pp. 543-551, April 2016.

[6] K. Meng, H. Yang, Y. Wang and D. Sun, "Modeling and Control of Single-Cell Migration Induced by a Chemoattractant-Loaded Microbead," IEEE Transactions on Cybernetics, vol. 49, no. 2, pp. 427-439, Feb. 2019.

[7] Z. Zhang, J. Huang, X. Wang, J. Liu, Y. Sun, "Robotic Immobilization of Motile Sperm for Clinical Intracytoplasmic Sperm Injection," IEEE Transactions on Biomedical Engineering, vol. 66, no. 2, pp. 444-452, Feb. 2019.

[8] S. Xiao, J. Riordon, M. Simchi, A. Lagunov, T. Hannam, K. Jarvi, R. Nosrati, D. Sinton. FertDish: microfluidic sperm selection-in-a-dish for intracytoplasmic sperm injection. Lab Chip.;vol. 21, no 4, pp:775-783, Feb. 2021.

[9] K. H. Campbell, J. McWhir, W. A. Ritchie, and I. Wilmut, " Sheep cloned by nuclear transfer from a cultured cell line," Nature, vol. 380, no. 6569, pp. 64, 1996.

[10] K. Malin, O. Witkowska, K. Papis . "The many problems of somatic cell nuclear transfer in reproductive cloning of mammals," Theriogenology. vol. 19, no. 1, pp:246-254, Jun 2022.

[11] T. Nguyen, T. -A. Tran, N. -Q. -K. Le, D. -M. Pham and Y. -Y. Ou, "An Extensive Examination of Discovering 5-Methylcytosine Sites in Genome-Wide DNA Promoters Using Machine Learning Based Approaches," IEEE/ACM Transactions on Computational Biology and Bioinformatics, vol. 19, no. 1, pp. 87-94, Feb. 2022.

[12] J. Zhou, Q. Lu, R. Xu, L. Gui and H. Wang, "EL_LSTM: Prediction of DNA-Binding Residue from Protein Sequence by Combining Long Short-Term Memory and Ensemble Learning," IEEE/ACM Transactions on Computational Biology and Bioinformatics, vol. 17, no. 1, pp. 124-135, Feb. 2020.

[13] K. Jung, A. Khan, R. Mocharnuk, S. Olivo-Marston, McDaniel JT. "Clinical encounter with three cancer patients affected by groundwater contamination at Camp Lejeune: a case series and review of the literature." J Med Case Rep, vol. 16, no. 1, pp: 272, Jul. 2022.

[14] H. Paik, J. Kim, S. Seo. "Analysis of the docking property of host variants of hACE2 for SARS-CoV-2 in a large cohort." PLoS Comput Biol. vol.18, no. 7, pp:834, Jul. 2022.

[15] A. H. Handyside, " Preimplantation genetic diagnosis, " Obstetrics, Gynaecology & Reproductive Medicine, vol. 21, no. 3, pp. 68-79, 2011.

[16] J. Yu, Q. Zhao, M. Cui, M. Sun and X. Zhao, "Robotic donor cell injection in Somatic Cell Nuclear Transfer (SCNT)," Proceeding of the 11th World Congress on Intelligent Control and Automation, 2014, pp. 2821-2825.
[17] D. Wen, L. A. Banaszynski, Z. Rosenwaks, C. D. Allis, and S. Rafii, " H3. 3 replacement facilitates epigenetic reprogramming of donor nuclei in somatic cell nuclear transfer embryos," Nucleus, vol. 5, no. 5, pp. 369-375, 2014.
[18] ,G. Shan, Z. Zhang, C. Dian, X. Wang and Y. Sun. "Model-Based Robotic Cell Aspiration: Tackling Nonlinear Dynamics and Varying Cell Sizes." IEEE Robotics and Automation Letters PP, no. 99 (2019): 1-1.
[19] X. P. Zhang, C. Leung, Z. Lu, N. Esfandiari, R. F. Casper and Y. Sun, "Controlled Aspiration and Positioning of Biological Cells in a Micropipette," IEEE Transactions on Biomedical Engineering, vol. 59, no. 4, pp. 1032-1040, April 2012.
[20] B. Liu. J., C. Shi, J. Wen, D. Pyne, H. Liu, C. Ru, J. Luo, S. Xie and A. Y. Sun. "Automated Vitrification of Embryos: A Robotics Approach," IEEE Robotics & Automation Magazine, vol. 22, no. 2, pp. 33-40, June 2015.
[21] Z. Zhang., J. Liu, X. Wang, Q. Zhao, C. Zhou, M. Tan, Sun, Y. "Robotic Pick-And-Place of Multiple Embryos for Vitrification," IEEE Robotics and Automation Letters, vol. 2, no. 2, pp. 570-576, April 2017.
[22] H. Yang, X. Li, Y. Liu and D. Sun, "Automated Transportation of Biological Cells for Multiple Processing Steps in Cell Surgery," IEEE Transactions on Automation Science and Engineering, vol. 14, no. 4, pp. 1712-1721, Oct. 2017.
[23] W. Shang, H. Lu, Y. Yang and Y. Shen, "7-DoFs Rotation-Thrust Microrobotic Control for Low-Invasive Cell Pierce via Impedance Compensation," IEEE/ASME Transactions on Mechatronics, doi: 10.1109/TMECH.2022.3173258.
[24] M. Sun, Y. Yao, X. Zhao, L. Li, H. Gong, J. Qiu, Y Liu. X Zhao,. "Precise Aspiration and Positioning Control Based on Dynamic Model Inside and Outside the Micropipette," in IEEE Transactions on Automation Science and Engineering, doi: 10.1109/TASE.2022.3153901.
[25] GAO Z. Scaling and bandwidth-parameterization based controller turning. Proceedings of fihe Americun Confirol Conference. Denver: IEEE 2003:4989-4996.
[26] D. Dong, W. S. Lam and D. Sun, "Electromagnetic Actuation of Microrobots in a Simulated Vascular Structure with a Position Estimator Based Motion Controller," IEEE Robotics and Automation Letters, vol. 5, no. 4, pp. 6255-6261, Oct. 2020.
[27] L. Zheng, Y. Jia, D. Dong, W. Lam, D. Li, H. Ji, Sun D. "3D Navigation Control of Untethered Magnetic Microrobot in Centimeter-Scale Workspace Based on Field-of-View Tracking Scheme," IEEE Transactions on Robotics, vol. 38, no. 3, pp. 1583-1598, June 2022.
[28] H. Marino, C. Bergeles and B. J. Nelson, "Robust Electromagnetic Control of Microrobots Under Force and Localization Uncertainties," IEEE Transactions on Automation Science and Engineering, vol. 11, no. 1, pp. 310-316, Jan. 2014.

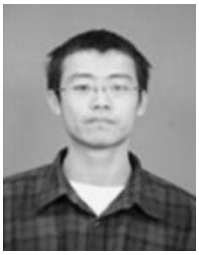

Xiangfei Zhao received the B. S. degree from Department of Wind Energy and Power Engineering, Hebei University of Technology, Tianjin, China, in 2013, the M.A. degree from the Automation College of Tianjin University of Technology, Tianjin, China, in 2017. He is currently working toward the Ph.D. degree in Control Theory and Control Engineering with the Nankai University, Tianjin, China. His current research interests include micromanipulation and micro/nanorobotics.

Mingzhu Sun (Member, IEEE) received the B.S., M.S., and Ph.D. degrees in computer science and technology, computer application, control theory and control engineering from Nankai University, Tianjin, China, in 2003, 2006, and 2009, respectively. Since 2009, she has been with the Institute of Robotics and Automatic Information System and the Department of Automation and Intelligence Science, Nankai University, Tianjin, China, She is an associator professor now. Her research interests are in micro-manipulator for life science, image processing and computer vision.

Qili Zhao (Member, IEEE) received the B. Eng. degree in Automation from Shandong University of Science and Technology, Tsingdao, China, in 2008, and the Ph.D. degree in Control Theory and Control Engineering from Nankai University, Tianjin, China in 2014. He finished his first postdoctoral research with the Robotics and Mechatronics Research Laboratory, Department of Mechanical and Aerospace Engineering, Monash University, Melbourne, Australia in 2014-2015. He finished his second postdoctoral research with Advanced Micro and Nanosystems Laboratory, Department of Mechanical and Industrial Engineering, Toronto University, Canada in 2015-2018. Now, he is an Assitant Proffessor in College of Artificial Intelligence, Nankai University. His research interests include robotic patch clamp system, automated drug screen, robotic cell manipulation and measurement.

Yaowei Liu (Member, IEEE) received the B.Eng. degree in automation and the Ph.D.
degree in control theory and control engineering from Nankai University, Tianjin, China, in 2013 and 2019, respectively. He is currently a Post-Doctoral Fellow with the College of Artificial Intelligence, Nankai University, Tianjin, China. He is also with Institute of Intelligence

Technology and Robotic Systems, Shenzhen Research Institute of Nankai University, Shenzhen, China. His research interests include micromanipulators and microsystems.

Yidi Zhang was born in 1997. She received the bachelor's degree in automation from Hebei University of Technology, Tianjin, China, in 2019. She is currently pursuing the Ph.D. degree with the school of Artificial Intellligence, Nankai University, Tianjin, China. Her current research interests include micromanipulation, micro-nano robotics.

Bingxin Li received the B.S. degree in automation from Shandong University, Jinan, China, in 2014, the M.S. degree in systems analysis and integration from Northeastern University, Shenyang, China, in 2017, and He is currently pursuing the Ph.D. degree in control science and engineering from Nankai University. His research interests include fractional order control systems, singular systems and robust control.

Xin Zhao (Member, IEEE) received th'e B.S. degree from Nankai University, Tianjin, China, in 1991, the M.S. degree from Shenyang Institute of Automation, CAS, Shenyang, China, in 1994, and the Ph.D. degree from Nankai University, in 1997, all in control theory and control engineering. He joined the faculty at Nankai University in 1997. He is a Professor and Secretary of the College of Artifificial Intelligence. His research interests are in micro manipulator, micro system and mathematical biology.